

Particle size distributions from small-angle scattering using global scattering functions

G. Beaucage,^{a,*} H. K. Kammler^b and S. E. Pratsinis^b

Received 29 December 2003

Accepted 15 April 2004

^aDepartment of Chemical and Materials Engineering, University of Cincinnati, Cincinnati, OH 45221-0012, USA, and ^bParticle Technology Laboratory, Department of Mechanical and Process Engineering, ETH Zürich, CH-8092 Zürich, Switzerland. Correspondence e-mail: beaucag@uc.edu

Control and quantification of particle size distribution is of importance in the application of nanoscale particles. For this reason, polydispersity in particle size has been the focus of many simulations of particle growth, especially for nanoparticles synthesized from aerosols such as fumed silica, titania and alumina. Single-source aerosols typically result in close to a log-normal distribution in size and micrograph evidence generally supports close to spherical particles, making such particles ideal candidates for considerations of polydispersity. Small-angle X-ray scattering (SAXS) is often used to measure particle size in terms of the radius of gyration, R_g , using Guinier's law, as well as particle surface area, S/V , from the Porod constant B and the scattering invariant Q . In this paper, the unified function is used to obtain these parameters and various moments of the particle size distribution are calculated. The particle size obtained from BET analysis of gas adsorption data directly agrees with the moment calculated from S/V . Scattering results are also compared with TEM particle-counting results. The potential of scattering to distinguish between polydisperse single particles and polydisperse particles in aggregates is presented. A generalized index of polydispersity for symmetric particles, $PDI = BR_g^4/(1.62G)$, where G is the Guinier prefactor, is introduced and compared with other approaches to describe particle size distributions in SAXS, specifically the maximum-entropy method.

© 2004 International Union of Crystallography
Printed in Great Britain – all rights reserved

1. Introduction

The polydispersity of nanoparticles is of importance in controlling properties related to their small size and high specific surface area. Additionally, the development of particle size distributions in the growth of nanoparticles has been a key feature of modelling and simulation for a number of years (Friedlander, 2000; Hinds, 1999). Current techniques for the determination of particle size distribution on the nanoscale can be categorized into transport-based measurements, such as differential mobility analysis and dynamic light scattering, physical property-based techniques, such as gas adsorption, and techniques for direct observation, such as transmission electron microscopy (TEM) of nanoparticles. TEM is probably the most widely applicable of the current techniques, though it is particularly tedious and subjective. Determination of primary particle size distributions for nanoparticles that are aggregated into mass-fractal structures is challenging due to the overlap of structural features.

Small-angle X-ray scattering offers the potential to resolve particle size distributions through a consideration of the scattered intensity over a wide range of size (scattering

vector). We have recently concentrated on ceramic nanoparticles produced in pyrolytic reactors. Such nanopowders are commonly encountered as fumed silica or titania. These materials are widely used as pigments and additives to a range of products, from plastics to food. In many cases, the primary particles from pyrolytic synthesis can be considered to be spherical. This is due to sintering of the particles and the dominance of coalescence at high temperature during pyrolytic growth.

Several groups have considered particle size distributions using SAXS. The simplest approach is to consider a distribution function, such as a Gaussian or log-normal particle size distribution, and to sum weighted scattering functions from simple structures, such as the sphere function. A fixed distribution function of this type can be locally minimized against scattering data to yield a particle size distribution. Such a solution, however, is not unique and any number of possible particle size distributions could describe a given scattering curve (unless the distribution is extremely narrow) (Bolze *et al.*, 2002; Dingenouts & Ballauff, 1999; Haubold *et al.*, 2003; Kranold *et al.*, 2003; Mulato & Chambouleyron, 1996; Mulato *et al.*, 1998; Nakamura *et al.*, 2003; Rieker, Hanprasopwattana *et al.*, 1999; Rieker, Misono & Ehrburger-Dolle, 1999; Martelli & Di Nunzio, 2002).

* On sabbatical leave to ETH Zürich.

Recently, a number of authors have considered a different approach to the description of particle size distribution from scattering based on algorithms native to image reconstruction: the maximum-entropy approach described by Skilling & Bryan (1984). This approach is usually based on spherical or ellipsoidal particles that display an arbitrary distribution of sizes. Rather than constraining the possible solutions by imposition of a distribution function, the solution with the largest value of ‘entropy’, as defined mathematically by Skilling & Bryan (1984), is chosen through an iterative procedure that maximizes the randomness of the solution while maintaining the square difference between the model and the data below a critical value associated with the statistics of the data. The maximum-entropy method is widely accepted as a reasonable approach to obtaining the most likely distribution function and it has been demonstrated to be effective at recreating a wide range of particle size distributions from model systems (Jemian *et al.*, 1991; Boukari *et al.*, 2000; Hansen, 1994; Morrison *et al.*, 1992; Potton *et al.*, 1988; Tagliani, 2000). Despite the success of the maximum-entropy approach, transformation of the scattering data leads to a disconnection between features observed in the scattering pattern and those seen in the size distribution. For instance, it is difficult to resolve features related to experimental or mathematical artifacts.

A more direct index of particle polydispersity would be a dimensionless parameter associated with the basic features directly observed in the scattering curve. The signature of polydispersity in scattering is the relationship between the Porod surface scattering regime at high magnitude, q , of the momentum transfer vector, q , and the Guinier regime at low q ,

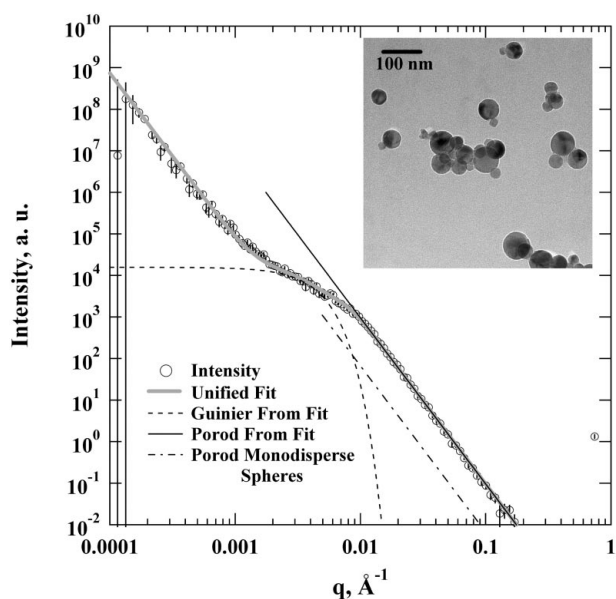


Figure 1 USAXS data (circles) from a non-fractal titania nanopowder. A unified fit (grey solid line) (Beaucage, 1995, 1996) and component curves of the unified function are shown. $d_{V/S} = 34.9$ nm (corrected to 41.3 nm), PDI = 14.4 ($\sigma_g = 1.60$), $R_g = 44.2$ nm, $2m_{SAXS} = 24.3$ nm, BET $d_p = 41.7$ nm, $2\langle R \rangle_{TEM} = 35$ nm, $2\langle R \rangle_{SAXS} = 27.2$ nm, $\sigma_{g,TEM} = 1.59$. The dot-dash line indicates Porod’s law for a sphere of identical R_g and G .

especially in the transition regime near $q \approx R_g^{-1}$ (Guinier & Fournet, 1955). For low-polydispersity spherical particles, in a log–log plot, this transition regime displays a distinct knee-like shape with the Porod scaling regime undershooting the Guinier regime in extrapolation (Fig. 1, dot–dash line). For high-polydispersity particles, this transition regime is a smooth curve with the Porod regime often overshooting the Guinier regime in extrapolation (Fig. 1, solid line). In addition to the qualitative advantage of a polydispersity index directly based on the shape of the scattering curve, such a polydispersity index, PDI, could be more robust and flexible in application than the use of an assumed distribution function or use of the maximum-entropy approach. For example, a generic PDI could be applied to mass-fractal aggregate scattering, while it is difficult to apply summed sphere functions or the maximum-entropy method to aggregate scattering since they must involve a choice of the q range to be used. An index of polydispersity could also easily be used to describe a series of samples with a single parameter directly related to the scattering data that could be plotted as a function of experimental conditions, for instance, regardless of changes in particle shape and distribution functions.

In the context of the previous paragraph, we should note that particles of moderate asymmetry (aspect ratio below 2) will show an identical signature in scattering as polydisperse spheres. For high-aspect-ratio particles, a separate scaling regime for the particle’s structural dimension, *i.e.* 1 for rods, 2 for disks, will be observed and the PDI might be used to calculate the dispersion in the smallest structural size, although these issues are beyond the scope of this article.

In this paper, the result of an analysis based on global scattering functions and a proposed polydispersity index will be compared with detailed TEM observations and gas adsorption measurements. Comparison will also be made between the maximum-entropy solution using a program developed by Jemian at NIST (Jemian *et al.*, 1991; Ilavsky, 2000) and distributions obtained using a polydispersity index based on the shape of the scattering curve as described by the three free parameters of global scattering functions for simple structures under the constraint of a log-normal distribution of spherical particles, discussed later.

2. Theory

2.1. Log-normal distribution

For pyrolytically synthesized particles, Fig. 1, particle growth is considered to begin with small, ~ 1 nm, highly polydisperse spherical particles (Sugimoto, 2000; Tsantilis *et al.*, 2001, 2002) in a reactive flame due to rapidly varying nucleation conditions. Through a combination of coalescence and sintering, these nuclei develop a narrower distribution at the early stages of flame growth, on the millisecond timescale (Kammler *et al.*, 2001; Friedlander, 2000). On the tens of milliseconds timescale, the dispersion in size will reach a self-preserving limit, usually considered to follow close to a log-normal distribution (Landgrebe & Pratsinis, 1990). In this

context, 'self-preserving' means that for timescales beyond the so-called self-preserving limit the median particle size continues to grow but the distribution maintains a relationship with the initial self-preserving distribution where a fixed geometric standard deviation is observed. That is, using time-dependent kinetic factors, such as the collision kernel, the distribution at later stages can be predicted from the self-preserving distribution. This greatly simplifies simulations and modelling of pyrolytic reactors, for instance. It is expected that nanoparticles collected from pyrolytic synthesis will generally follow a log-normal distribution (Hinds, 1999) although exceptions to this behavior are known, particularly when insufficient residence time above a critical sintering temperature exists (Kammler *et al.*, 2003). Additionally, the particle size distribution can broaden when particles are collected from different stream-lines in a flame, with different temperature and residence-time histories.

One advantage of the log-normal distribution, $f(R)$, is that all moments of this distribution can be calculated using a simple non-integral relationship that requires only two free parameters, m and σ :

$$f(R) = \frac{1}{R\sigma(2\pi)^{1/2}} \exp\left\{-\frac{[\log(R/m)]^2}{2\sigma^2}\right\}, \quad (1)$$

where R is the particle size, in this case, $f(R)$ is the number distribution, and m is related to the mean by $\langle R \rangle = m \exp(\sigma^2/2)$. The r th moment of the log-normal distribution is given by

$$\langle R^r \rangle = m^r \exp(r^2\sigma^2/2) = \exp(r\mu + r^2\sigma^2/2), \quad (2)$$

where $\mu = \ln m$ (Evans *et al.*, 1993, p. 102). The geometric mean radius, x_g is given by $\exp m$, and the geometric standard deviation is given by $\sigma_g = \exp \sigma$ (Crow & Shimizu, 1988, p. 333). The geometric mean is the value with the greatest frequency for a log-normal distribution, *i.e.* the median particle radius. For a monodisperse distribution, $\sigma = 0$. Using equation (2), the log-normal distribution can be estimated from two moments of the distribution. It should be noted that equation (1) yields a number distribution as a function of radius and must be multiplied by KR^3 to obtain the volume distribution, where K is a normalization constant. In the plots below, the volume distribution is plotted *versus* the particle diameter, $2R$.

2.2. Global scattering function, the unified equation

Fig. 1 gives a scattering pattern obtained at the UNICAT facility of the Advanced Photon Source in Chicago, IL, using a Bonse-Hart ultra-small-angle X-ray-scattering camera. The sample is non-aggregated titania with a particle size measured by BET analysis of gas adsorption of 41.7 nm. The mean size from TEM is 35 nm ($2\langle R \rangle_{\text{SAXS}} = 27.2$ nm) and the geometric standard deviation, σ_g , from TEM is 1.59. The scattered intensity is plotted as a function of the scattering vector, q , which is related to the scattering angle, θ , by $q = (4\pi/\lambda)\sin(\theta/2)$, where λ is the wavelength. The data are presented on a log-log scale to emphasize power-law regimes

such as are observed at high q in the Porod regime for the particle surface scattering,

$$I(q) = Bq^{-4}, \quad B = 2\pi r_e^2 N \rho_e^2 S, \quad (3)$$

where S is the average surface area for a primary particle and N is the number density of primary particles. ρ_e is the average electron density difference between a primary particle and air, and r_e is the classical electron radius. (The data are in arbitrary units since the sample thickness, of about 0.2 mm, has not been used to normalize the data.) At lower q ($q \simeq 0.004 \text{ \AA}^{-1}$), a transition region is observed that reflects the limit of surface scattering at the average primary particle size, R_g , as described by Guinier's law,

$$I(q) = G \exp(-q^2 R_g^2/3), \quad G = N r_e^2 \rho_e^2 V^2, \quad (4)$$

where V is an average particle volume. At lowest q , in Fig. 1, a second Porod regime, equation (3), is observed with a smaller surface area compared with the high- q Porod regime, since the Porod constant, B , has a lower value.¹ These larger particles (lower q) are clusters of primary particles, termed soft agglomerates to distinguish them from nanoscale aggregates or hard agglomerates as discussed later. Previously it was observed that soft agglomerates can be broken apart when nanoscale particles are dispersed in polymers, for instance, while aggregates (or hard agglomerates) remain only slightly affected by such processing (Kohls & Beaucage, 2001). Different behavior is observed for carbon black, which does not have ionically bonded primary particles (Rieker *et al.*, 2000).

These local scattering laws, equations (3) and (4), are directly used in the global unified scattering function (Beaucage, 1995, 1996),

$$I(q) = G \exp\left(\frac{-q^2 R_g^2}{3}\right) + B(q^*)^{-4}, \quad q^* = \frac{q}{[\text{erf}(qR_g/6^{1/2})]^3}, \quad (5)$$

where $\text{erf}()$ is the error function and equation (5) is written for a single polydisperse level of structure, such as for polydisperse spherical primary particles. Equation (5) can be extended for any number of related or unrelated levels of structure, as described by Beaucage (1996) for mass-fractal aggregates.

In Fig. 1, it is clear that the global fit to the scattering data, the unified fit, can distinguish Guinier regimes where significant overlap with the Porod regime(s) occurs. For monodisperse spherical particles, the Porod power law intercepts the Guinier curve at a higher q than a tangent to the Guinier curve of -4 power law. A population of monodisperse spheres corresponds with the smallest possible surface area, B , for a given particle size, R_g , and volume. Polydispersity, as well as asymmetry, of the particles serves to increase the dimension-

¹ For three-dimensional agglomerates of particles, the Porod prefactor $B_2 = (2\pi G_2/V_2)(S/V)_2$, following equations (3) and (4). For the nanoparticles, $B_1 = (2\pi G_1/V_1)(S/V)_1$. Then a lower value of B_2 relative to B_1 indicates that the agglomerates have a lower surface area than the primary particles, since $G_2/G_1 = z$, where z is the number of particles in an agglomerate, and since $V_2 = zV_1$ for three-dimensional agglomerates, so $B_2/B_1 = (S/V)_2/(S/V)_1$.

less ratio of BR_g^4/G . This ratio, normalized by the value for monodisperse spheres of 1.62 (the lowest possible value), serves as an index for polydispersity, PDI. The sample shown in Fig. 1 displays a polydispersity greater than the log-normal self-preserving limit of aerosol growth (Friedlander, 2000), where $PDI = 5.56$ as discussed below, indicating that maturation of nanoparticles during growth was truncated due to insufficient residence time at high temperatures in the flame. For such a sample, it is only possible to determine the mean particle size using a global scattering function because of the significant overlap between the Guinier and Porod regimes (Beaucage, 1995, 1996).

The data in Fig. 1 are on an arbitrary scale and it is an advantage of the PDI approach that the value can be obtained from intensity of arbitrary units since the scaling of intensity affects both B and G through a scaling constant that cancels in the ratio of B/G .

2.3. B , G , R_g for monodisperse spheres

For monodisperse spheres,

$$G = Nr_c^2 \rho_c^2 V^2 = \frac{16\pi^2}{9} Nr_c^2 \rho_c^2 R^6 = Nr_c^2 \rho_c^2 \frac{2000\pi^2}{243} R_g^6, \quad (6)$$

while

$$B = 2\pi Nr_c^2 \rho_c^2 S = 8\pi^2 Nr_c^2 \rho_c^2 R^2 = \frac{40\pi^2 Nr_c^2 \rho_c^2 R_g^2}{3}, \quad (7)$$

yielding

$$B = \frac{81G}{50R_g^4} = \frac{1.62G}{R_g^4}. \quad (8)$$

The same function can be obtained directly from the global scattering formula for monodisperse spheres (Guinier & Fournet, 1955),

$$I(R, q) = G \left\{ \frac{3[\sin(qR) - qR \cos(qR)]}{(qR)^3} \right\}^2 = \frac{9G[\sin^2(qR) - 2qR \sin(qR) \cos(qR) + (qR)^2 \cos^2(qR)]}{(qR)^6}. \quad (9)$$

At high q , the oscillating terms can be approximated by their average, $\langle \cos^2 qR \rangle = \langle \sin^2 qR \rangle = \frac{1}{2}$, and $\langle \sin qR \cos qR \rangle = 0$, yielding

$$I(R, q) \Rightarrow \frac{9G[1/2 - 0 + (qR)^2/2]}{(qR)^6} \Rightarrow \frac{9G}{2(qR)^4} = \frac{81G}{50(qR_g)^4} = \frac{1.62G}{R_g^4} q^{-4}, \quad (9a)$$

with $(5/3)^{1/2} R_{g,\text{sphere}} = R$. Then, a factor of 1.62 is again obtained for the ratio BR_g^4/G .

2.4. B , G , R_g and moments of the particle size distribution for polydisperse spheres

Under the assumption of spherical particles, the three scattering fit parameters, B , G and R_g , can be related to

moments of the particle size distribution (Sjoberg, 1974; Moller *et al.*, 1995; Damaschun *et al.*, 1969). From equation (6) we have

$$G = Nr_c^2 \rho_c^2 \langle V^2 \rangle = Nr_c^2 \rho_c^2 \left(\frac{4\pi}{3} \right)^2 \sum_0^\infty n_i(R) R_i^6 = Nr_c^2 \rho_c^2 \left(\frac{4\pi}{3} \right)^2 \langle R^6 \rangle, \quad (6a)$$

where

$$\langle R^p \rangle = \sum_0^\infty n_i(R) R_i^p. \quad (10)$$

N represents the total number density of particles in the number density distribution, $n(R)$. For a system with a total particulate volume fraction φ and irradiated volume V_s , the total number of particles, NV_s , is given by

$$NV_s = V_s \varphi / \left[\sum n_i(R) V_i \right] = V_s \varphi / [(4/3)\pi \langle R^3 \rangle]. \quad (11)$$

Then G , equation (6a), is proportional to the ratio of $\langle R^6 \rangle / \langle R^3 \rangle$. This function is used, for instance, in the determination of the weight-average molecular weight for polymers using solution light scattering, where $R^6 \simeq M^2$ and $R^3 \simeq M$, so $M_w = \langle M^2 \rangle / \langle M \rangle$ (Roe, 2001).

As a direct consequence of the Guinier power series for intensity (Guinier & Fournet, 1955), $I(q) = Nr_c^2 \rho^2 V^2 (1 - q^2 R_g^2/3 + \dots) \simeq G \exp(-q^2 R_g^2/3)$, for a polydisperse system (Roe, 2001, p. 170) we consider that R_g^2 is weighted by V^2 where V is the particle volume. As shown by Roe (2001) and Moller *et al.* (1995), for spherical particles,

$$R_g^2 = \frac{\sum_0^\infty n_i(R) v_i^2 R_{gi}^2}{\left[\sum_0^\infty n_i(R) v_i^2 \right]} = \frac{3}{5} \frac{\sum_0^\infty n_i(R) R_i^8}{\left[\sum_0^\infty n_i(R) R_i^6 \right]} = \frac{3\langle R^8 \rangle}{5\langle R^6 \rangle}. \quad (12)$$

Also, for spheres,

$$B = 2\pi r_c^2 N \rho_c^2 \langle S \rangle = 8\pi^2 r_c^2 N \rho_c^2 \sum_0^\infty n_i R_i^2 = 8\pi^2 r_c^2 N \rho_c^2 \langle R^2 \rangle, \quad (13)$$

and B is proportional to $\langle R^2 \rangle / \langle R^3 \rangle$ through the normalization constant, following the same reasoning as equations (6a) and (11). Then B/G is given by

$$B/G = 9\langle R^2 \rangle / (2\langle R^6 \rangle). \quad (14)$$

Assuming polydisperse spheres, three moments can be directly obtained from the parameters needed to reconstruct a single level of scattering, $\langle R^2 \rangle$ from B , $\langle R^6 \rangle$ from G , and $\langle R^8 \rangle$ from R_g^2 and G . Integrals of the scattering curve can yield a number of higher order moments, as described by Moller *et al.* (1995) (see also Dekany & Turi, 1998; Fenistein & Barre, 2001; Sheu, 1992; Sjoberg, 1974). For example, the Porod invariant, Q , yields an additional moment of importance to the comparison with gas adsorption measurements, as described below.

Table 1

Values of $R_g^4 B / (1.62G)$, the spherically normalized PDI, for various functions.

Functions: 1 from Roe (2001) or Guinier & Fournet (1955); 2, 6 and 7 from Evans *et al.* (1993); 6 also from Crow & Shimizu (1988); 4 and 5 from Friedlander (2000); 8 from Higgins & Benoit (1994).

Distribution	$R_g^4 B / (1.62G)$
Monodisperse spheres ¹	1.00
Block distribution ²	1.41
Intercept Porod/Guinier ³	3
Log-normal self-preserving continuum regime ⁴	4.93
Log-normal self-preserving free-molecular regime ⁵	5.56
Log-normal (spheres) ⁶	$\exp(12\sigma^2)$
Most probable ⁷	8.70
Debye–Bueche function ⁸	9.88

If the scattered intensity is integrated over all scattering angles for a particular structure, such as the primary particles in an aggregate, the invariant that pertains to the scattering power of the structure can be obtained:

$$Q = \int_0^\infty q^2 I(q) dq = 2\pi^2 r_c^2 N V \rho_c^2 = 2\pi^2 r_c^2 N \rho_c^2 K_{\text{shape}} \langle R^3 \rangle = \frac{8}{3} \pi^3 r_c^2 N \rho_c^2 \langle R^3 \rangle_{\text{sphere}}, \quad (15)$$

where K_{shape} depends on the particle shape. Comparison of equations (3), (13) and (15) shows that the ratio of the Porod invariant, Q , and the Porod power-law prefactor, B , can yield a particularly important moment of the particle size distribution: the surface to volume ratio. This ratio does not depend on particle symmetry, *i.e.* a spherical assumption is not necessary. The agreement between this ratio and ratios predicted assuming spherical particles and a fixed distribution function are an internal check for the appropriateness of the assumed symmetry, usually the spherical assumption, and the distribution function. That is, $K_{S/V}$ in equation (16) can be calculated for spheres, for instance, to yield a low-moment spherical-equivalent diameter:

$$\frac{\pi B}{Q} = \frac{\langle S \rangle}{\langle V \rangle} = K_{S/V} \frac{\langle R^2 \rangle_{\text{sphere}}}{\langle R^3 \rangle} \rightarrow \frac{6}{d_{V/S}}, \quad (16)$$

where ‘6’ is a constant associated with the surface to volume ratio for a sphere, and a factor of 2 to convert radius to diameter. Additionally, the ratio can be directly compared with the particle size determined by BET analysis of gas adsorption data, d_p (Kammler *et al.*, 2004), as well as with TEM image analysis. Using a global scattering function such as the unified function, the Porod invariant can be calculated directly from the fit parameters using only the parts of the scattering curve that pertain to the primary particles, so that particle correlations associated with the mass-fractal structure are not included in the integral for primary-particle size (Beaucage & Schaefer, 1994).

The invariant can also be used to determine the mean volume associated with the ratio for the sixth and third moments (Moller *et al.*, 1995), $2\pi^2 G/Q = \langle V \rangle = 4\pi \langle R^6 \rangle / (3 \langle R^3 \rangle)$.

Integrals of $I(q)q^n$ have been related to a number of other moments by Moller *et al.* (1995).

It should be noted that since the lowest order moment directly obtained from scattering is $\langle R^3 \rangle / \langle R^2 \rangle$, calculation of lower order moments such as the mean and median, although possible, must involve an extrapolation from the observed data. Then it is preferable to compare scattering results with higher order moments.

2.5. Log-normal distribution for polydisperse spheres

For polydisperse spheres, the two parameters needed to describe the log-normal distribution, m and σ , can be obtained directly from the three unified fit parameters, through the unitless ratio BR_g^4/G and R_g . The spherically normalized PDI, $BR_g^4/(1.62G)$, is directly related to σ ,

$$\ln \sigma_g = \sigma = \left\{ \frac{\ln [B(R_g^2)^2 / (1.62G)]}{12} \right\}^{1/2} = \left(\frac{\ln \text{PDI}}{12} \right)^{1/2} \quad (17)$$

and

$$m = \{5R_g^2 / [3 \exp(14\sigma^2)]\}^{1/2}, \quad (18)$$

using equations (2), (6a), (12), (13) and alternatively (14), where σ_g is the geometric standard deviation.² m is the median radius so the median diameter is $2m$. Similarly, the mean diameter is $2\langle R \rangle$, equation (2).

The self-preserving limit for pyrolytic aerosol growth is reached when $\sigma_g = 1.44$, for the continuum regime of particle transport, and 1.46, for the free-molecular regime of particle transport (Friedlander, 2000, p. 217). Since $\sigma_g = \exp \sigma$, these two limits correspond with $\sigma = 0.365$ and 0.378, respectively. For spherical particles in the continuum regime at the self-preserving limit, $BR_g^4/G = 7.99$, and for the free-molecular regime $BR_g^4/G = 9.00$ in the self-preserving limit, as noted in Table 1. Distinguishing between free-molecular and continuum self-preserving limits from SAXS data is generally close to the limit of resolution; however, the approach to these limits from highly polydisperse particles is easily resolved, as discussed later in this article.

Values for the dimensionless index of polydispersity, BR_g^4/G , are given in Table 1 for a variety of possible situations. The intercept value corresponds with the condition where the Porod power-law decay just intercepts the Guinier scattering curve. This value is smaller than the log-normal self-preserving limits, but larger than the value for monodisperse spheres, serving as an indicator for polydispersity since this relative value for B can be easily extrapolated graphically in a log intensity *versus* $\log q$ plot. The monodisperse sphere value is the absolute minimum of this ratio, 1.62. The Debye–Bueche function corresponds to the value for the Debye–Bueche

² Equation (17) can be obtained by using equation (2) for the moments in equation (14), thereby obtaining a relationship between G/B , m and σ . Equation (12) can be used in the same way with equation (2) to obtain an expression relating R_g , m and σ . In the ratio of $(R_g^2)^2 B/G$, from these expressions, m^4 cancels and an expression relating PDI to σ is obtained [equation (17)]. Equation (18) is obtained directly from the expanded equation (12).

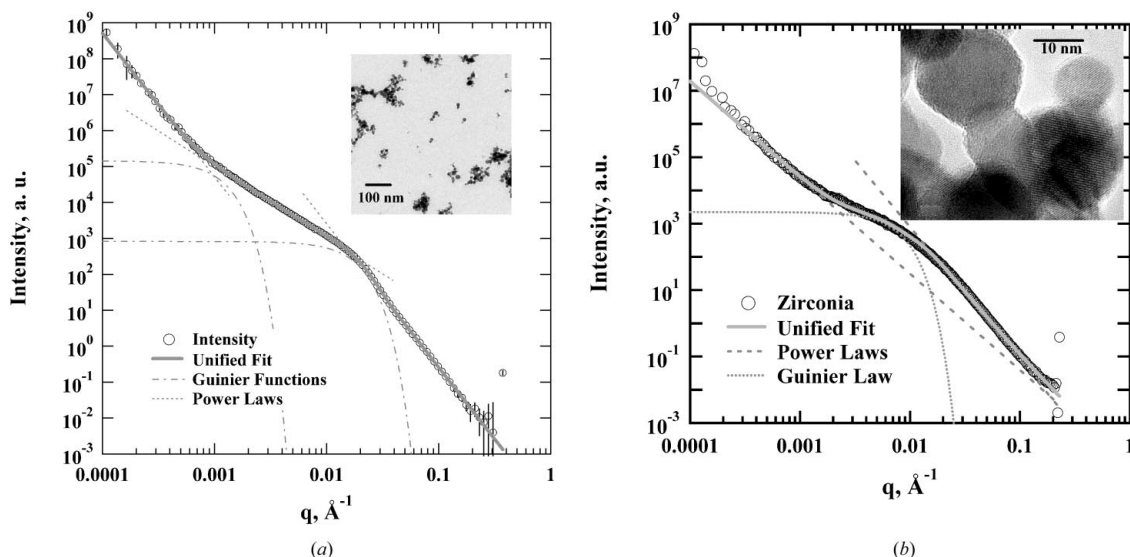


Figure 2

USAXS data from aggregated nanoparticles (circles) showing unified fits (bold grey lines), primary particle Guinier and Porod functions at high q , the intermediate mass fractal scaling regime and the aggregate Guinier regime (dashed lines). (a) Fumed titania sample with multi-grain particles and low- q excess scattering due to soft agglomerates. $d_{V/S} = 16.7$ nm (corrected to 18.0 nm), PDI = 3.01 ($\sigma_g = 1.35$), $R_g = 11.2$ nm, $d_f = 1.99$, $z_{2:1} = 175$, $z_{R_g} = 226$, $R_{g2} = 171$ nm. From gas adsorption, $d_p = 16.2$ nm. (b) Fumed zirconia sample (Mueller *et al.*, 2004) with single-grain particles, as shown in the inset. The primary particles for this sample have high polydispersity leading to the observed hump near the primary particle scattering regime. $d_{V/S} = 20.3$ nm, PDI = 10.8 ($\sigma_g = 1.56$), $R_g = 26.5$ nm, $d_f = 2.90$. From gas adsorption, $d_p = 19.7$ nm.

scattering function for structures displaying an exponential correlation function (Debye & Bueche, 1949*a,b*). It is interesting that this value is higher than that for any typical distribution. The most probable value corresponds to the most probable distribution (Evans *et al.*, 1993). This is an exponential distribution function and the value for the polydispersity index is close to that for the Debye–Bueche function.

The polydispersity index of Table 1 is useful as a direct estimate of polydispersity from the scattering curve and is independent of assumed distribution functions and particle shape. It can be used directly to calculate a log-normal standard deviation for spherical particles assuming a log-normal distribution, equation (17). It is also possible to calculate asymmetry factors using the PDI, although this is not discussed here. The PDI can be directly compared with model values (Table 1) in order to gauge the approach to a theoretical particle size distribution, such as the self-preserving limit in nanoparticle growth. Additionally, the intercept value (Table 1) can be easily interpreted qualitatively in a scattering graph to judge between high- and low-polydispersity samples.

2.6. Mass-fractal aggregates

An advantage of global scattering functions, such as the unified function, is that overlapping scaling regimes can be distinguished using least-squares fitting routines. Fig. 2 shows a typical USAXS scattering pattern from aggregated nanoparticulate titania. The high- q structural level (Guinier and Porod regime) is somewhat obscured by the intermediate- q mass-fractal scaling regime that follows a power-law scaling of

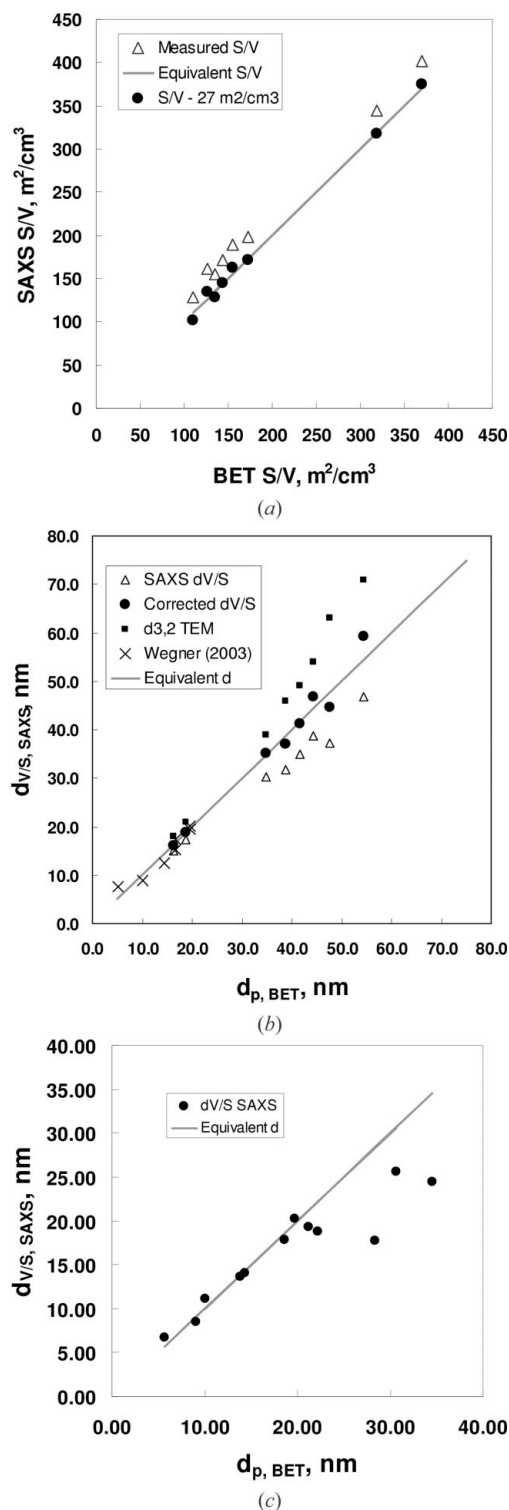
$$I(q) = B_f q^{-d_f}, \quad (19)$$

where d_f is the mass fractal dimension for an average aggregate defining the relationship between mass, M_{agg} and size, R_{agg} ,

$$M_{agg} = \alpha R_{agg}^{d_f}, \quad (20)$$

and α is the lacunarity, which is generally of the order of 1 for aerosol particles (Friedlander, 2000). For determination of the surface to volume ratio, and $d_{V/S}$, from the Porod invariant, only the highest- q structural level is considered from such a system, as was previously demonstrated (Beaucage & Schaefer, 1994). Similarly, the unified function can be used to discriminate the contribution to scattering from the primary particles and to use this calculated contribution to determine the polydispersity index, PDI, of Table 1.

For mass-fractal scattering, Figs. 2(a) and 2(b), a power-law regime of weak slope, between 1 and 3, is observed for q smaller than the primary-particle Guinier regime, equation (4). In most cases there is a continuous transition between the mass-fractal power-law scattering and the primary-particle Guinier regime. For aggregates with unusually high primary-particle polydispersity, Fig. 2(b), $q \simeq 0.015 \text{ \AA}^{-1}$, a distinct ‘hump’ in the scattering curve occurs at the primary particle Guinier regime, where the primary Guinier scattering is larger than the extrapolated mass-fractal power-law scattering. This hump is due to the dependence of scattered intensity on R^6 through the squared volume term of equation (6a), so that the largest particles of a wide distribution dominate the scattering. In Fig. 2(a), PDI = 3.01 ($\sigma_g = 1.35$), which is lower than the self-preserving limit of $\text{PDI}_{SPL} = 5.56$ ($\sigma_{g,SPL} = 1.46$), while in Fig. 2(b), PDI = 10.8 ($\sigma_g = 1.56$), much higher than the self-preserving limit.


Figure 3

(a) S/V from SAXS for titania particles produced by vapor-phase pyrolysis of titania tetraisopropoxide by Kammler *et al.* (2002, 2003). The SAXS S/V can be made to agree with the BET value by subtraction of $27 \text{ m}^2 \text{ cm}^{-3}$. (b) $d_{V/S}$ from USAXS [and corrected from (a)] versus d_p from BET analysis of gas adsorption data for a series of titania samples produced by Kammler (triangles and filled circles), and samples made in a quenched-spray flame from Wegner & Pratsinis (2003) (crosses, single-grain particles). The calculated $d_{3,2}$ from TEM micrographs for the Kammler samples is also shown (filled squares). (c) $d_{V/S}$ from USAXS versus d_p from BET for fumed zirconia samples of Mueller *et al.* (2004).

Mass-fractal aggregates are described by the dimension d_f , in equations (19) and (20), the degree of aggregation, z , and the branch content. From a general perspective, the branch content cannot be determined in static measurements, although consideration of the overall shape of aggregate scattering patterns may contain information concerning branching. The degree of aggregation, z , reflects the number of primary particles in an average aggregate. This can be obtained in several ways from the parameters fitted to scattering data, as follows.

(a) z can be obtained directly from the ratio of the Guinier prefactors for the aggregate and primary levels of structure, G_2/G_1 (Beaucage, 1996), which reflects a low-order moment of z since $G_1 \simeq \langle z \rangle$ and $G_2 \simeq \langle z^2 \rangle$.

$$z_{2,1} = G_2/G_1 = \langle z^2 \rangle / \langle z \rangle, \quad (21)$$

where the power of z is associated with the source moments. This calculation involves no assumptions concerning the aggregate structure, except that the particles described by G_1 aggregate to form the structure described by G_2 .

(b) z can be estimated from the radii of gyration from the two levels of structure,

$$z_{R_g} = (R_{g,2}^2/R_{g,1}^2)^{d_f/2} = (\langle z^{2+2/d_f} \rangle / \langle z^2 \rangle)^{d_f/2}, \quad (22)$$

under the assumption that R_g is a direct measure of size both for the primary particles and for the aggregates. This assumption is paramount to an assumption of a narrow distribution in both aggregate and primary size. Equation (22) reflects a higher order moment than equation (21), *i.e.* a larger value. The moment ratio in equation (22) is obtained from the Guinier power series, $I(q) = Nr_c^2 \rho^2 V^2 (1 - q^2 R_g^2/3 + \dots)$, where $\rho^2 V^2 = n_c^2 \simeq z^2$ for an aggregate, and $R_{g,2}^2 \simeq z^{2/d_f}$. Then $\langle R_{g,2}^2 \rangle$ is proportional to $\langle z^{2+2/d_f} \rangle / \langle z^2 \rangle$ in analogy to equation (12). For $d_f = 2$, $z_{R_g} = (R_{g,2}^2/R_{g,1}^2) = \langle z^3 \rangle / \langle z^2 \rangle$, for instance, while for a rod, $d_f = 1$ and $z_{R_g} = (R_{g,2}^2/R_{g,1}^2)^{1/2} = (\langle z^4 \rangle / \langle z^2 \rangle)^{1/2}$.

3. Results and discussion

3.1. $d_{V/S}$ and d_{BET}

In the work of Kammler *et al.* (2004), excellent agreement between $d_{V/S}$, equation (16), and d_p , obtained using BET analysis of gas adsorption data, was observed for amorphous silica nanoparticles across a wide range of size. In contrast, the samples measured in Fig. 3 are crystalline nanoparticles of titania (Figs. 3a and 3b) and zirconia (Fig. 3c). The samples shown in Figs. 3(a) and 3(b) are produced by pyrolysis of titanium tetraisopropoxide, TTIP, in a methane/oxygen premixed flame, as reported by Kammler *et al.* (2002, 2003) with the exception of the Wegner samples (crosses, Fig. 3b), which were produced in a quench-nozzle spray flame as described by Wegner & Pratsinis (2003). The intent of the quench nozzle is to lock-in early states of structural growth in the flame, and the Wegner particles are much smaller than those from the premixed flame of Kammler. In general, the smaller primary particles tend to bond into mass-fractal aggregates, while the larger primary particles are typically

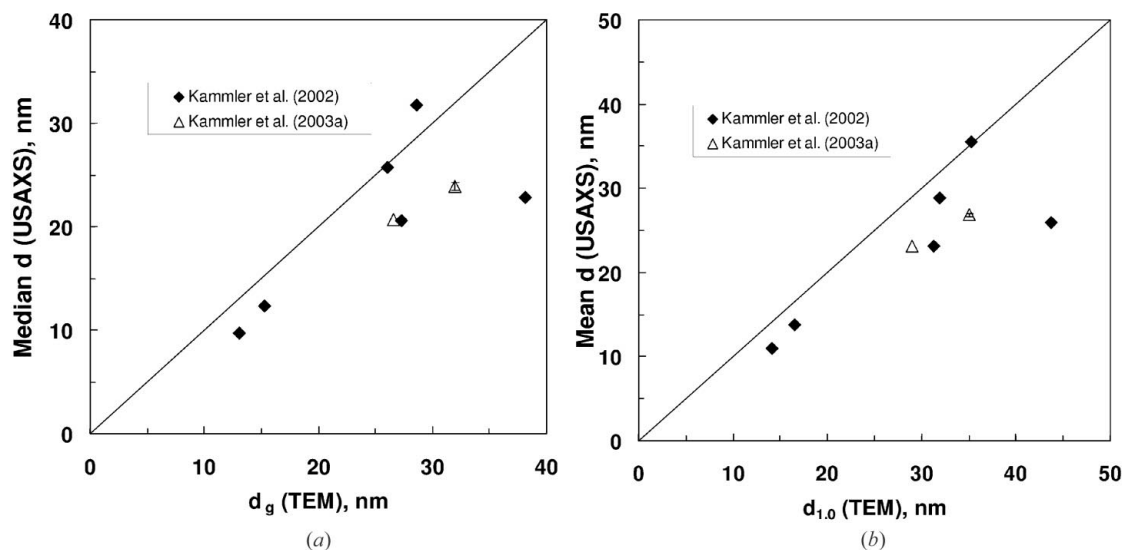


Figure 4 (a) Comparison of the median particle size from *expm*, with *m* defined by equation (18), and the median particle size calculated from an analysis of TEM data on TiO₂. (b) Mean particle size, $\langle R \rangle$ from USAXS, equation (2) with $r = 1$, and from TEM (Kammler *et al.*, 2003) for the same samples as Figs. 3(a) and 3(b).

non-aggregated. The crystalline titania powders of Fig. 3(b), hollow triangles, do not show good agreement with d_p from gas adsorption measurements, with $d_{V/S} < d_p$.

This deviation for these non-faceted spherical particles (see inset to Fig. 1) may be associated with the grainy nature of the titania particles, which may lead to an erroneously high specific surface area in SAXS and a correspondingly lower V/S ratio. Some support for this internal structure is seen in the inset to Fig. 1. The internal structure could also be associated with internal pores, which would result in an indistinguishable reduction in $d_{V/S}$ compared with d_p . Fig. 3(a) shows a possible correction to such data where a constant value of $27 \text{ m}^2 \text{ cm}^{-3}$ has been subtracted from the SAXS S/V values, leading to agreement between BET and SAXS (solid circles). A constant value of this correction factor indicates an internal closed pore or grain structure which does not vary with particle size. By converting these corrected S/V values, the corrected $d_{V/S}$ values in Fig. 3(b) are obtained. The Wegner particles (crosses in Fig. 3b) do not contain grain boundaries (Wegner & Pratinis, 2003) and yield much better agreement between SAXS and BET.

It should be noted that Kammler (Kammler *et al.*, 2003) reports good agreement between X-ray diffraction (XRD) peak width analysis based on the Scherrer equation and d_p from gas adsorption. However, such agreement is not expected for single-grain polydisperse powders, since the XRD peak width should reflect a higher order moment ratio than d_p and a correspondingly larger value. For instance, a Debye–Waller Gaussian peak function (Debye, 1913; Waller, 1923) would result in $d_{\text{XRD}}^2 \simeq \langle R^8 \rangle / \langle R^6 \rangle$ following the logic used to obtain equation (12). For polydisperse multi-grain particles, d_{XRD} will bear a complicated relationship to other moments of the particle size distribution.

Fig. 3(c) shows results from zirconia powder produced by Mueller *et al.* (2004) in a spray flame. Fig. 2(b) shows a typical fit to SAXS from these mass-fractal powders. Mueller’s

powders are single grained with no internal structure (inset to Fig. 2b) and agreement between d_p and $d_{V/S}$ is seen, similar to that found for amorphous silica by Kammler *et al.* (2004). The three largest particles in Fig. 3(c) show a lower $d_{V/S}$ than that expected from gas adsorption (higher S/V), which might be associated with internal closed pores for the larger particles.

3.2. Comparison with TEM analysis

Fig. 4 compares low-order moments, (a) the median and (b) the mean from USAXS and TEM for the samples of Fig. 3 (Kammler *et al.*, 2002, 2003). The median is calculated from TEM micrographs assuming a log-normal size distribution so that the geometric mean diameter is equal to the count median diameter (Hinds, 1999). The median for USAXS is obtained from *expm* using equation (18). The TEM median seems to be generally higher than the USAXS value. The mean $\langle R \rangle$ from equations (1), (2), (17) and (18) is shown in Fig. 4(b) as a function of the mean calculated from TEM micrographs for the same samples. Again, the mean size is generally lower for the USAXS analysis. As noted above, values of lower order moments from USAXS, such as the median and mean (Fig. 4), are probably less accurate than those from TEM analysis since the SAXS pattern is primarily related to higher order moments, equations (9), (13) and (15). Similar agreement is seen between $d_{V/S}$ from SAXS and from TEM particle size distribution curves (Fig. 3b, solid squares).

3.3. Particle size distributions by TEM, PDI/ R_g and maximum-entropy method

Fig. 5(a) shows two USAXS measurements on the same titania powder (two samples) which were measured from different sample preparations in order to estimate the reproducibility of the entire USAXS analysis of particle size distributions. The unified fit to one of the samples is shown along with the two component curves from which the poly-

dispersity index, PDI (Table 1), is determined. The sample is from a TTIP flame producing 3.1 g h^{-1} of titania (identical to Fig. 1) with non-aggregated particles. Fig. 5(b) shows the resulting particle size distributions obtained by (a) particle counting from TEM micrographs (circles), and two methods of analysis of the USAXS data, (b) assuming a log-normal distribution and using equations (1), (2), (17) and (18), as well as (c) using the maximum-entropy routine of Jemian (Jemian *et al.*, 1991; Skilling & Bryan, 1984). There is good agreement between the results for the two measurements and analyses. The TEM evaluation (circles) may indicate at least three modes to the distribution which are ignored in the log-normal approach (grey lines). The maximum-entropy routine shows three major modes and in some cases can reproduce the major details of the TEM analysis (Figs. 5, 6 and 7). The reprodu-

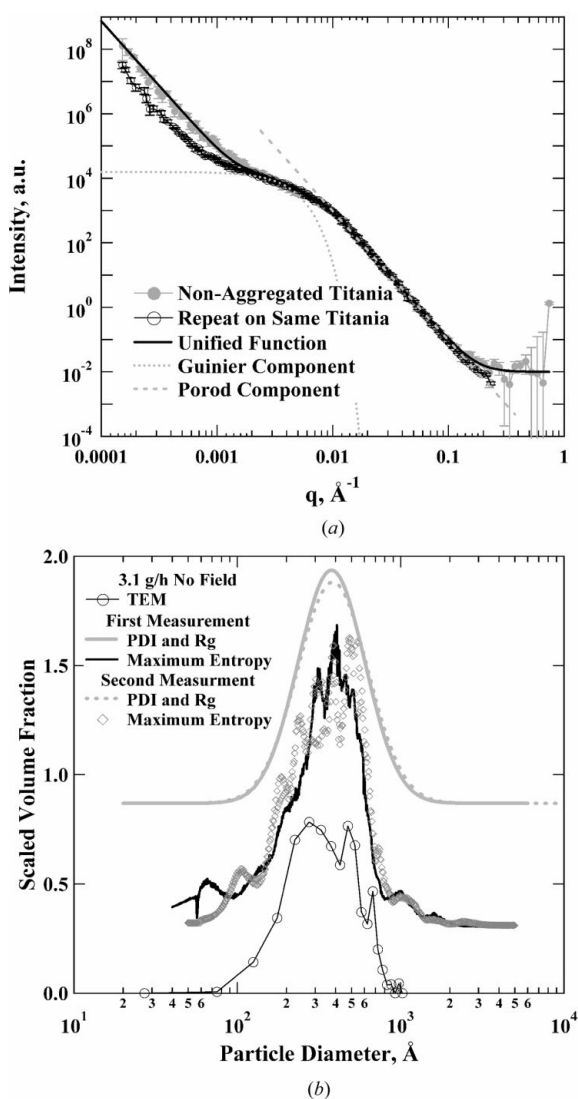


Figure 5
 3.1 g h^{-1} titania. (a) Repeat USAXS runs on a non-aggregated titania powder (Fig. 1). (b) Particle size distributions from TEM (circles; Kammler *et al.*, 2003), equations (1), (2), (17) and (18) using PDI and R_g , and using the maximum-entropy program of Jemian (Jemian *et al.*, 1991). Distribution curves are shifted vertically for clarity. $d_{V/S} = 34.9 \text{ nm}$, PDI = 14.4 ($\sigma_g = 1.60$), $R_g = 44.2 \text{ nm}$.

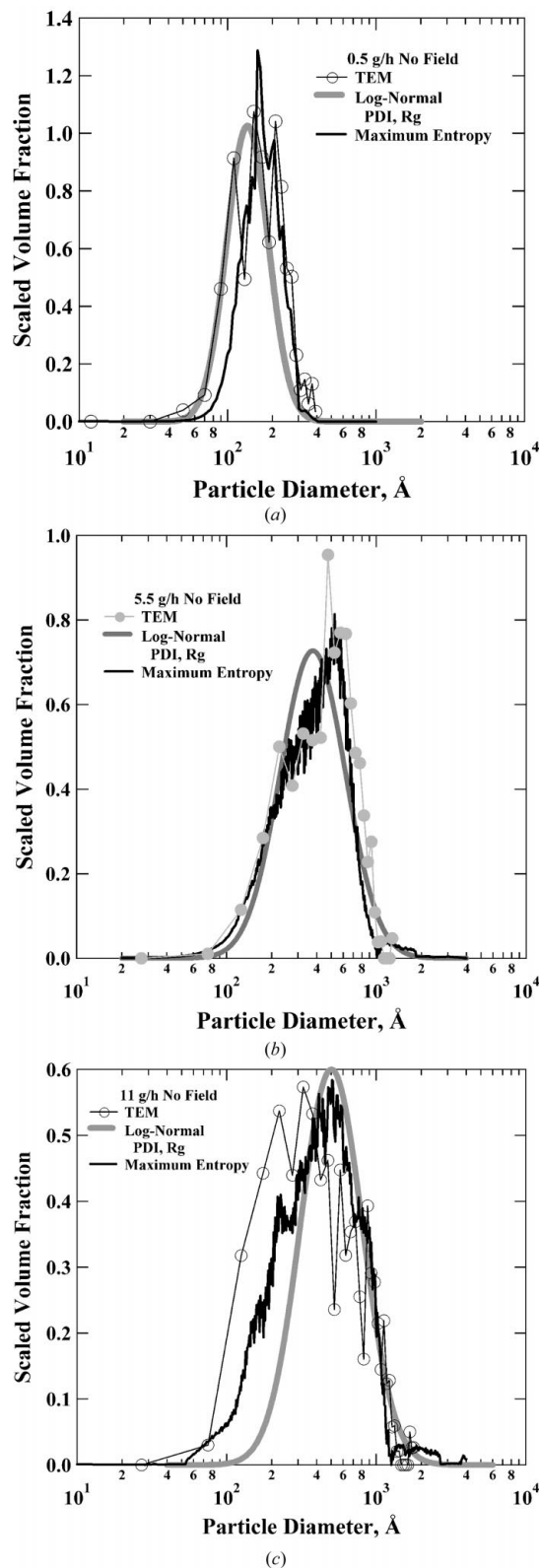


Figure 6
 Comparison of particle volume distributions for titania made without an electric field using TEM (circles; Kammler *et al.*, 2003), PDI (grey line) and maximum entropy (black line). (a) 0.5 g h^{-1} [fractal $d_{V/S} = 12.1 \text{ nm}$, PDI = 3.52 ($\sigma_g = 1.38$), $R_g = 8.9 \text{ nm}$, $d_t = 1.59$, $z_{2:1} = 1160$, $z_{R_g} = 1343$]. (b) 5.5 g h^{-1} [$d_{V/S} = 37.2 \text{ nm}$, PDI = 20.0 ($\sigma_g = 1.65$), $R_g = 50.8 \text{ nm}$]. (c) 11 g h^{-1} [$d_{V/S} = 46.8 \text{ nm}$, PDI = 15.5 ($\sigma_g = 1.61$), $R_g = 60.8 \text{ nm}$]. (3 g h^{-1} is shown in Fig. 5.)

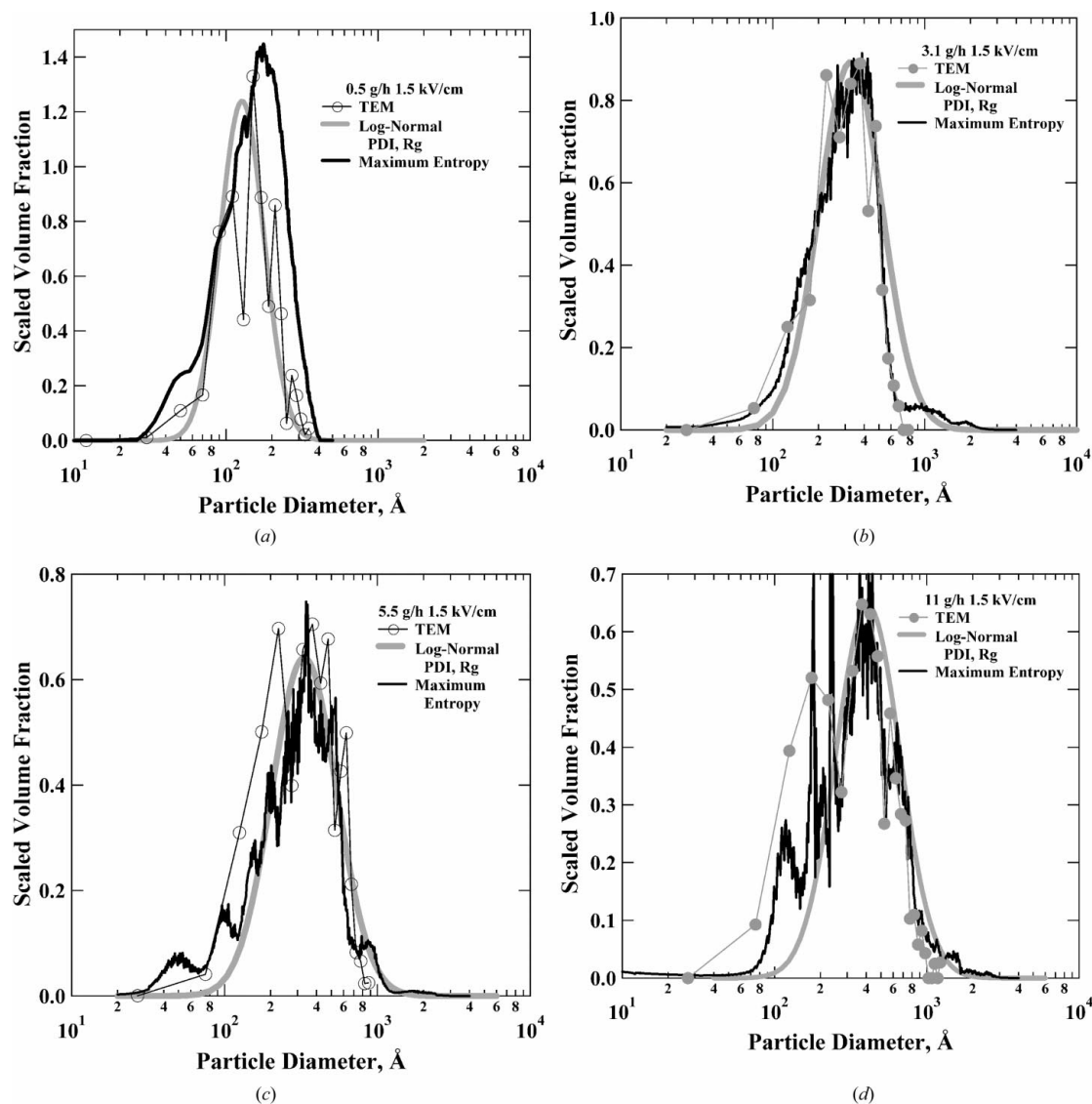


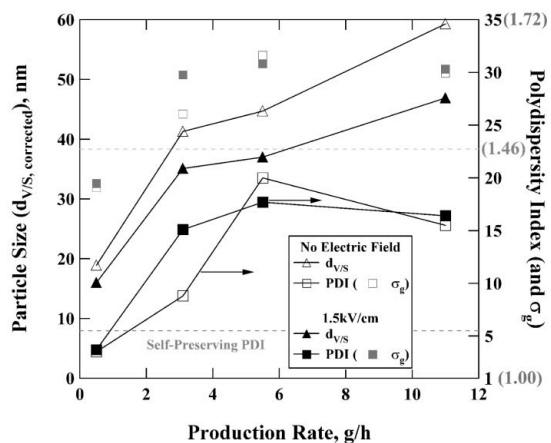
Figure 7 Comparison of particle volume distributions for titania made with an electric field of 1.5 kV cm^{-1} using TEM (circles; Kammler *et al.*, 2003), PDI (grey line) and maximum entropy (black line). (a) 0.5 g h^{-1} [fractal $d_{V/S} = 10.9 \text{ nm}$, PDI = 3.7 ($\sigma_g = 1.39$), $R_g = 8.5 \text{ nm}$, $d_t = 1.71$, $z_{2:1} = 18.1$, $z_{R_g} = 28.7$]. (b) 3.1 g h^{-1} [$d_{V/S} = 30.3 \text{ nm}$, PDI = 15.1 ($\sigma_g = 1.61$), $R_g = 39.0 \text{ nm}$]. (c) 5.5 g h^{-1} [$d_{V/S} = 31.7 \text{ nm}$, PDI = 17.7 ($\sigma_g = 1.63$), $R_g = 42.5 \text{ nm}$]. (d) 11 g h^{-1} [$d_{V/S} = 38.7 \text{ nm}$, PDI = 16.4 ($\sigma_g = 1.62$), $R_g = 51.0 \text{ nm}$].

cibility of the particle size distribution is fairly good in Fig. 5(b). Again, differences may be associated with powder inhomogeneity, although the raw SAXS data sets seem to be extremely close for the two samples except for soft-agglomerate scattering at lowest q and background scattering at the highest q . Soft agglomerates are weakly bonded, so it is not surprising to observe variability in the low- q region of the scattering curve.

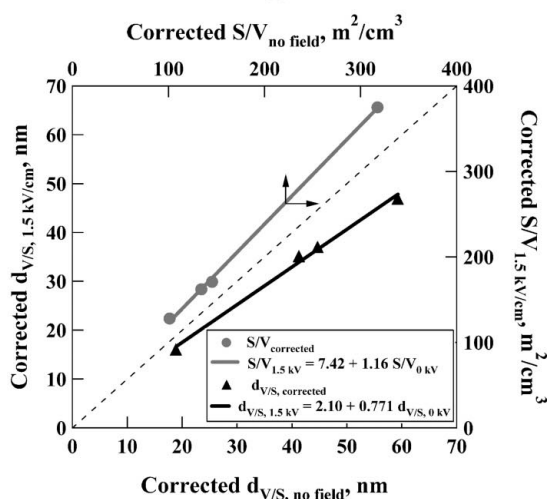
Figs. 6 and 7 show particle size distributions from a series of titania samples produced at variable production rates and with and without an electric field of 1.5 kV cm^{-1} applied near the burner in the particle stream, as previously reported (Kammler *et al.*, 2003). The smallest particles (0.5 g h^{-1} with and without an electric field) are aggregated, while the majority of the particles are non-aggregated. For fractal

aggregates, the high- q portion of the data related to the primary particles was transformed using the maximum-entropy method. This resulted in a reasonable match between TEM, PDI/ R_g and maximum-entropy results. It should be noted that obtaining the particle size distribution using TEM from mass-fractal aggregates is more difficult than for non-aggregated particles and we expect an enhanced count at large sizes due to the potential of over counting agglomerates of smaller particles in the TEM analysis (Figs. 6a and 7a).

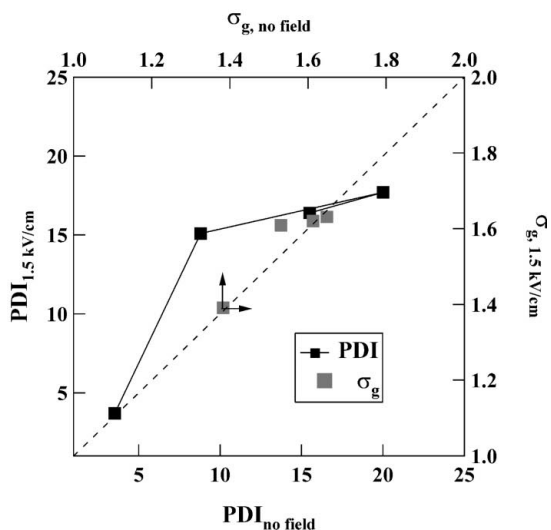
Generally, the maximum-entropy solution agrees with TEM analysis while the log-normal results agree in terms of general shape with both the TEM and maximum-entropy size-distribution curves. Fig. 8(a) shows a plot of the corrected $d_{V/S}$ (triangles) and PDI (black squares with line) versus production rate, summarizing Figs. 5, 6 and 7. The first two points,



(a)



(b)



(c)

Figure 8

(a) Particle size, $d_{V/S}$ (triangles), and spherically normalized polydispersity index, PDI (squares with line), versus production rate for titania flames with and without an electric field. σ_g , assuming spherical particles and a log-normal distribution, is also shown on a linear scale with bracketed values on the right-hand axis (squares with no line). (b) $d_{V/S}$ and S/V with 1.5 kV cm^{-1} versus no field, showing linear behavior. (c) Effect of field on particle size distribution: PDI and σ_g with field versus without field.

$d_{V/S} < 20 \text{ nm}$, correspond to primary particles in fractal aggregates, while the remaining particles are non-aggregated. σ_g , from equation (17), is shown as grey squares with values on a linear scale shown in parentheses on the right-hand axis. The σ_g values are based on assumptions of a log-normal distribution and spherical particles that are fairly good for these powders, while the PDI values are independent of assumptions concerning shape and particle size distribution. PDI is directly related to the scattering curve as discussed above, while σ_g is more detached from the observed data.

The behavior seen in Fig. 8(a) is associated with a shorter residence time and higher flame temperature at higher production rates. For the low flow rates, particles have sufficient time to reach the self-preserving distribution, $\text{PDI} \approx 5.5$ ($\sigma_g = 1.46$). Additional residence in the flame at temperatures near the minimum temperature for sintering, high in the flame, leads to mass-fractal aggregates, since complete coalescence cannot occur. At higher flow rates, the reduction in residence time and high temperature ensure large particles that do not reach the self-preserving limit in size distribution. At the highest flow rates, the flame temperature is high enough to lead to a reduction in the width of the particle size distribution despite the shortened residence time. The presence of an electric field reduces the particle size, especially at high production rates, as previously reported (Kammler *et al.*, 2003), but has little effect on the particle size distribution. The reduction in particle size due to the applied field is surprisingly manifested by a proportional increase in the specific surface area, as seen in Fig. 8(b), with $S/V_{1.5 \text{ kV cm}^{-1}} = 7.4 \text{ m}^2 \text{ cm}^{-3} + 1.2 S/V_{\text{no field}}$ as a best fit. This may be related to surface charge effects in the presence of the field, which leads to about a 20% increase in specific surface area. Fig. 8(c) shows no similar trend in PDI or σ_g .

4. Conclusion

Nanoparticles produced in pyrolytic synthesis are widely used in industry and research. Such particles rarely display monodisperse size and often aggregate into mass-fractal structures. Small-angle X-ray scattering is a useful technique to characterize these nanoparticles. Since scattering involves measurement on small size scales of large collections of these particles, it is natural to consider particle size distributions. Generally, small-angle X-ray scattering yields high-order moments of the particle size distribution, with the most commonly used measure of size, the radius of gyration, reflecting the ratio of the eighth to the sixth moment of size, so the radius of gyration is extremely sensitive to the population of largest particles. A more useful measure of size can be obtained from the surface to volume ratio. This size, $d_{V/S}$, was shown to agree with gas adsorption measurements and with calculations from transmission electron micrographs.

An index of polydispersity is proposed for SAXS data based on the ratio of the Porod constant, B , times R_g^4 and divided by the Guinier prefactor, G . This ratio has a minimum value of 1.62 for monodisperse spheres, by which it can be normalized, and increases with increasing polydispersity (and particle

shape asymmetry). The PDI is directly related to σ_g for a log-normal distribution of spheres. The advantages of this polydispersity index over distribution-based direct fits to scattering data are as follow.

(i) The PDI allows for an interpretation of scattering data by inspection.

(ii) The PDI is independent of distribution functions. The PDI can be adapted to various distribution functions after the scattering data have been analyzed.

(iii) Through comparison of PDI-generated log-normal distributions with data transforms, such as the maximum-entropy method, erroneous features in the particle size distribution generated by mathematical routines, such as additional modes, can be identified.

(iv) The PDI provides an analytic dimensionless number to which an error value can be directly assigned from the statistical error in the scattering data. Such a number is of use in directly comparing and identifying trends for a series of data, regardless of changes in the actual distribution function or particle shape.

The PDI was demonstrated both for mass-fractal aggregates and non-aggregated nanoparticles. USAXS and TEM data for spherical nanoparticles were compared. The particle size distributions were calculated by assuming spherical primary particles and a log-normal distribution, and these were compared with a direct transform of the scattering data using the method of maximum entropy proposed by Skilling & Bryan (1984), as well as with the particle size distributions obtained from TEM. Generally, agreement was seen between the three methods. Finally, we suggested a generic plot of d_{VIS} and PDI for a series of samples for which experimental conditions vary, e.g. production rate and electric field. Such a plot allows a direct comparison of a series of nanopowders in terms of two simple parameters that are independent of assumptions, such as the form of the size distribution and particle shape, and which are directly related to the observed scattering curve.

We gratefully acknowledge the support of the National Science Foundation (CTS-0070214), the Swiss National Science Foundation (200021-101901/1), the Swiss Commission for Technology and Innovation (TopNano21-5487.1) and the synchrotron facilities at UNICAT/APS. We thank J. Ilavsky and P. Jemian for experimental assistance. GB thanks the University of Cincinnati for a sabbatical leave to ETH Zentrum. The UNICAT facility at the Advanced Photon Source (APS) is supported by the US DOE under Award No. DEFG02-91ER45439, through the Frederick Seitz Materials Research Laboratory at the University of Illinois at Urbana-Champaign, the Oak Ridge National Laboratory (US DOE contract DE-AC05-00OR22725 with UT-Battelle LLC), the National Institute of Standards and Technology (US Department of Commerce) and UOP LLC. The APS is supported by the US DOE, Basic Energy Sciences, Office of Science under

contract No. W-31-109-ENG-38. R. Mueller and R. Jossen are thanked for providing zirconia samples.

References

- Beaucage, G. (1995). *J. Appl. Cryst.* **28**, 717–728.
 Beaucage, G. (1996). *J. Appl. Cryst.* **29**, 134–146.
 Beaucage, G. & Schaefer, D. W. (1994). *J. Non-Cryst. Solids*, **172**, 797–805.
 Bolze, J., Peng, B., Dingenouts, N., Panine, P., Narayanan, T. & Ballauff, M. (2002). *Langmuir*, **18**, 8364–8369.
 Boukari, H., Long, G. G. & Harris, M. T. (2000). *J. Colloid Interface Sci.* **229**, 129–139.
 Crow, E. L. & Shimizu, K. (1988). Editors. *Log Normal Distributions: Theory and Practice*. New York: Marcel Deker.
 Damaschun, G., Moller, J. J., Porschell, H.-V. & Sommer, G. (1969). *Monatsh. Chem.* **100**, 1701–1714.
 Debye, P. (1913). *Verh. Dtsch. Phys. Ges.* **15**, 738–752.
 Debye, P. & Bueche, A. M. (1949a). *J. Appl. Phys.* **20**, 518–525.
 Debye, P. & Bueche, A. M. (1949b). *Phys. Rev.* **75**, 1308.
 Dekany, I. & Turi, L. (1998). *Colloid Surf. A*, **133**, 233–243.
 Dingenouts, N. & Ballauff, M. (1999). *Langmuir*, **15**, 3282–3288.
 Evans, M., Hastings, N. & Peacock, B. (1993). *Statistical Distributions*, 2nd ed. New York: John Wiley.
 Fenistein, D. & Barre, L. (2001). *Fuel*, **80**, 283–287.
 Friedlander, S. K. (2000). *Smoke, Dust and Haze: Fundamentals of Aerosol Dynamics*. Oxford University Press.
 Guinier, A. & Fournet, G. (1955). *Small-Angle Scattering of X-rays*. New York: John Wiley.
 Hansen, S. (1994). *Acta Cryst.* **A50**, 547–550.
 Haubold, H.-G., Vad, T., Waldofner, N. & Bonnemann, H. (2003). *J. Appl. Cryst.* **36**, 617–620.
 Higgins, J. S. & Benoit, H. C. (1994). *Polymers and Neutron Scattering. Oxford Series on Neutron Scattering in Condensed Matter* 8. Oxford: Clarendon Press.
 Hinds, W. C. (1999). *Aerosol Technology*, 2nd ed. New York: John Wiley.
 Ilavsky, J. (2000). *Particle Size Distribution from USAXS, A Manual for USAXS Analysis*, UNICAT, Argonne Illinois, USA, <http://www.uni.aps.anl.gov>.
 Jemian, P. R., Weertman, J. R., Long, G. G. & Spal, R. D. (1991). *Acta Metall. Mater.* **39**, 2477–2487.
 Kammler, H. K., Beaucage, G., Mueller, R. & Pratsinis, S. E. (2004). *Langmuir*, **20**, 1915–1921.
 Kammler, H. K., Jossen, R., Morrison, P. W. Jr, Pratsinis, S. E. & Beaucage, G. (2003). *Powder Technol.* **135–136**, 310–320.
 Kammler, H. K., Mädler, L. & Pratsinis, S. E. (2001). *Chem. Eng. Technol.* **24**, 583–596.
 Kammler, H. K., Pratsinis, S. E., Morrison, P. W. & Hemmerling, B. (2002). *Combust. Flame*, **128**, 369–381.
 Kohls, D. J. & Beaucage, G. (2001). *Curr. Opin. Solid State Mater. Sci.* **6**, 183–194.
 Kranold, R., Kriesen, S., Haselhoff, M., Weber, H.-J. & Goerigk, G. (2003). *J. Appl. Cryst.* **36**, 410–414.
 Landgrebe, J. D. & Pratsinis, S. E. (1990). *J. Colloid Interface Sci.* **139**, 63–86.
 Martelli, S. & Di Nunzio, P. E. (2002). *Particle Particle Syst. Char.* **19**, 247–255.
 Möller, J., Kranold, R., Schmelzer, J. & Lembke, U. (1995). *J. Appl. Cryst.* **28**, 553–560.
 Morrison, J. D., Corcoran, J. D. & Lewis, K. E. (1992). *J. Appl. Cryst.* **25**, 504–513.
 Mueller, R., Jossen, R., Pratsinis, S. E., Watson, M. & Akhtar, M. K. J. (2004). *Am. Ceram. Soc.* **87**, 197–202.
 Mulato, M. & Chambouleyron, I. (1996). *J. Appl. Cryst.* **29**, 29–36.
 Mulato, M., Tygel, D. & Chambouleyron, I. (1998). *J. Appl. Cryst.* **31**, 149–153.

- Nakamura, K., Kawabata, T. & Mori, Y. (2003). *Powder Technol.* **131**, 120–128.
- Potton, J. A., Daniel, G. J. & Rainford, B. D. (1988). *J. Appl. Cryst.* **21**, 663–668.
- Rieker, T. P., Hanprasopwattana, A., Datye, A. & Hubbard, P. (1999). *Langmuir*, **15**, 638–641.
- Rieker, T. P., Hindermann-Bischoff, M. & Ehrburger-Dolle, F. (2000). *Langmuir*, **16**, 5588–5592.
- Rieker, T. P., Misono, S. & Ehrburger-Dolle, F. (1999). *Langmuir*, **15**, 914–917.
- Roe, R. J. (2001). *X-ray and Neutron Scattering from Polymers*. New York: Academic Press.
- Sheu, E. (1992). *Phys. Rev. A*, **45**, 2428–2438.
- Sjöberg, G. (1974). *J. Appl. Cryst.* **7**, 192–199.
- Skilling, J. & Bryan, R. K. (1984). *Monthly Notices R. Astronom. Soc.* **211**, 111–124.
- Sugimoto, T. (2000). *Monodisperse Particles*. New York: Elsevier.
- Tagliani, A. (2000). *Appl. Math. Comput.* **112**, 333–343.
- Tsantilis, S., Briesen, H. & Pratsinis, S. E. (2001). *Aerosol Sci. Technol.* **34**, 237–246.
- Tsantilis, S., Kammler, H. K. & Pratsinis, S. E. (2002). *Chem. Eng. Sci.* **57**, 2139–2156.
- Waller, I. (1923). *Z. Phys.* **17**, 398–408.
- Wegner, K. & Pratsinis, S. E. (2003). *AIChE J.* **49**, 1667–1675.